A. Kumar, S. Ramasamy, S. Padmanaban and G. Gatto, "Implementation of Energy Management Strategy for Solar PV-Fed Hybrid Systems Using High-Gain DC–DC Converter and Transformerless Inverter," in *IEEE Transactions on Consumer Electronics*, vol. 72, no. 1, pp. 291-302, Feb. 2026.

The publisher's version is available at:

http://dx.doi.org/10.1109/TCE.2026.3653581

Implementation of Energy Management Strategy for Solar PV-Fed Hybrid Systems Using High-Gain DC–DC Converter and Transformerless Inverter

Amit Kumar, *Member, IEEE*, Suganthi Ramasamy, *Member, IEEE*, Sanjeevikumar Padmanaban, *Senior Member, IEEE*, and Gianluca Gatto, *Senior Member, IEEE*

Abstract*—This paper proposes an integrated energy management system for solar photovoltaic (PV) fed hybrid power configurations that combines a high-gain DC-DC converter with a battery storage unit and a transformerless H-bridge inverter. The proposed architecture eliminates isolation transformers, enhancing system efficiency and compactness. This research suggests the development of a switched inductor–capacitor–based high-gain converter that achieves a maximum voltage gain, operating efficiently at lower duty cycles and reduced component stress. The power management strategy employs a Maximum Power Point Tracking (MPPT) controller to regulate the DC link voltage under dynamic irradiance and load conditions. This approach ensures effective power balancing between the generation and load sides through bi-directional power flow, supporting stable operation during sudden fluctuations in solar input. The system's performance is validated through extensive simulations in MATLAB/Simulink and experimental testing. Compared to existing converter configurations, the proposed method achieves a peak system efficiency of 97.7%, resulting in reduced power losses and enhanced voltage regulation. The energy management algorithm responds in real time to power deviations. Simulation and hardware results confirm the robustness of the configuration under both steady-state and dynamic scenarios, supporting its sustainability for consumer-grade PV hybrid systems.

***Index Terms*—High-gain DC-DC converter, DC link inverter voltage control, hybrid power management, battery storage unit.**

I. Introduction

SOLAR photovoltaic (PV) technology is beneficial because of its ability to harness virtually inexhaustible and sustainable energy from sunlight, while minimizing environmental impact and the resource-intensive extraction processes associated with it. Solar PV systems are increasingly favored over wind power because of their compact size, cost-effectiveness, and widespread availability [1], [2].

In high-PV power generation systems, the generated power is fed into the AC grid through the power conversion system. Typically, DC-DC conversion and DC-AC power conversion are used in PV systems to ensure stable and efficient power export to the grid [3], [4]. To guarantee a steady and uninterrupted power supply, power conversion circuits and additional power sources are necessary to maintain consistent power delivery. However, in the dual conversion stage, high-power losses have been occurring in solar PV systems [5], [6].

To reduce power losses in solar PV systems, transformerless converters with a reduced number of devices have been developed in recent years [7]. Additionally, to extract maximum power and ensure stable operation, various Maximum Power Point Tracking (MPPT) techniques have been explored, and different energy management strategies have been developed with an energy storage system [8], [9].

In single-stage conversion systems, the inverter and controller are integrated directly into the power generation to the load. However, these systems often suffer high power losses because of the larger number of switching devices. This system also incorporates complex control techniques to maintain DC link voltage stability [10], [11]. On the other hand, two-stage PV conversion systems employ a DC-DC converter to stabilize the DC link voltage before the inverter stage, thereby simplifying control requirements and improving system efficiency [12].

Numerous studies have focused on non-isolated DC-DC converters for boosting the DC link voltage in solar PV systems, thereby eliminating the need for step transformers [13], [14], [15], [16]. However, conventional boost converters experience high conduction losses and switching stress at maximum duty cycles [17]. While three-port non-isolated converters offer high power density for maintaining a constant DC link voltage, they are often plagued by high magnetic losses because of the passive and active components [18], [19], [20]. Correspondingly, coupled inductor high-gain DC converters were developed to achieve voltage gain. Still, this configuration suffers from voltage spikes caused by leakage inductance, leading to increased power dissipation and noise [21], [22], [23]. To optimize power export to the grid, various MPPT algorithms are employed for the DC-DC converter under varying solar irradiance conditions. The Modified Invasive Weed Optimization (MIWO) algorithm not only ensures maximum power transfer to the grid but also mitigates fluctuations in the DC link voltage [24]. The Firefly Algorithm-Particle

Amit Kumar, Suganthi Ramasamy, and Gianluca Gatto are with the Department of Electrical and Electronic Engineering, University of Cagliari, 09123 Cagliari, Italy (e-mail: amit.kumar@unica.it; suganthi.ramasamy@unica.it).

Sanjeevikumar Padmanaban is with the Department of Electrical Engineering IT and Cybernetics, University of South-Eastern Norway, 3679 Porsgrunn, Norway.

Swarm Optimization (FA-PSO) is developed to reduce DC link voltage fluctuations and minimize power variations in the DC microgrid. However, this algorithm exhibits limitations in controlling the periodicity [25]. To improve convergence time, the Modified Adaptive Jaya Optimization (MAJO) is proposed to regulate power flow variations in solar power systems. Implementing this algorithm is more complex when applied to experimental test setups [26].

To address these limitations, switched capacitor and voltage multiplier cell configurations have been investigated to achieve higher voltage gains [27], [28]. However, these approaches often require numerous components and multiple stages, which can degrade overall system efficiency [29], [30]. In the secondary AC-DC conversion stage, traditional inverter configurations are extensive, space-consuming, and costly. Recent advancements in transformerless inverter configurations, such as the H-7 topology, have demonstrated improved efficiency with fewer devices and simpler control techniques [31], [32], [33], [34]. The H-7 inverter, when combined with Modified Discontinuous Pulse Width Modulation (MDPWM) techniques, offers superior efficiency on the AC side [35], [36], [37].

Despite these advancements, considerable potential remains for research in developing new circuit topologies that offer maximum voltage gain with enhanced performance. This study examines a high-voltage gain DC-DC converter designed to improve the performance of non-isolated converters [38], [39]. The proposed converter employs a diode-capacitor cell configuration, followed by switched inductor circuitry, to achieve maximum gain at lower duty cycles, thereby reducing device stress and improving overall efficiency. The integrated load management system maintains a stable DC link voltage, ensuring balanced power delivery under changing environmental conditions.

Recent studies have also advanced PV battery integration with predictive control, optimization, and high-gain converter innovations. For example, grid-forming inverters with model-free predictive control have improved stability [40]. Metaheuristic algorithms such as Chef-Based Optimization (CBOA) have been employed for tracking the global peak power in PV systems [41]. High-gain DC-DC converters with soft switching and reduced components have been demonstrated for compact consumer applications [42]. Single-input dual-output converters for DC microgrids further extend their functionality [43]. Similarly, adaptive MPPT strategies for portable EV chargers highlight the importance of efficiency under dynamic load and irradiance conditions [44]. While these state-of-the-art works focus on either control robustness or converter topology, they often lack a unified design that combines high-gain conversion, transformerless inverter operation, and State of Charge (SoC) aware PV battery energy management with explicit validation of DC-link stability. The present work addresses this gap by proposing a co-designed high-gain DC-DC converter and H-7 transformerless inverter with an integrated Energy Management System (EMS), validated through both simulation and a 2.5 kW hardware prototype.

Additionally, this manuscript analyzes the performance of a DC-DC converter-fed H-7 transformerless inverter configuration combined with the MDPWM technique. The proposed research work is structured in this paper as follows: Section II analyzes the various modes of operation for the high-gain DC-DC converter with the MPPT technique. Additionally, this section compares the performance of the proposed high-gain converter with that of existing converter topologies. The operation of the MPPT controller is also covered. Section III presents the energy management algorithm, H-7 transformerless configuration, MDPWM technique, and power flow control strategies. Comprehensive analysis and MDPWM operations are detailed in this section. Section IV provides a thorough analysis of power control management through simulation studies. Finally, Section V presents the experimental validation and results of the proposed research work.

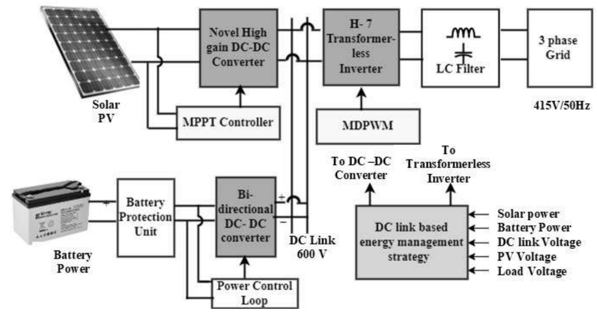

Fig. 1. Generalized block diagram of solar PV-fed hybrid system.

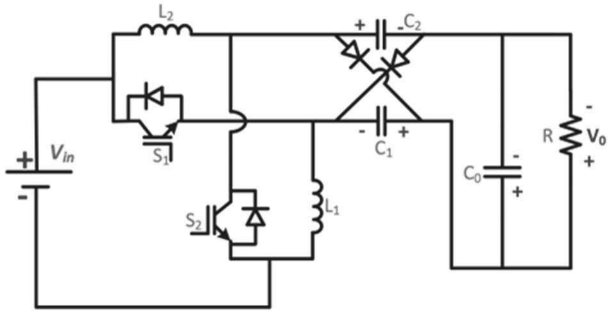

Fig. 2. Proposed Switched Inductor–Capacitor High-gain generation side converter.

II. Hybrid Power Management Topology

Fig. 1 illustrates the fundamental structure of a PV and battery storage-fed hybrid topology featuring a transformerless DC converter and H-7 inverter configuration.

An additional bidirectional converter, along with a battery unit and a power management strategy, is also employed to maintain system stability. Further, to achieve THD reduction, an LC filter has been designed and connected on the load side.

A. Proposed High-Voltage Gain Generation-Side DC-DC Converter

In both grid-connected and off-grid solar PV systems, the DC-link voltage is typically low. However, the DC-AC conversion process requires a high and stable DC-link voltage. To carry out the MPPT function to increase the DC voltage level in a low-voltage solar PV system, an additional DC-DC converter is required. The primary method for boosting the voltage of PV panels for a constant DC link of the inverter

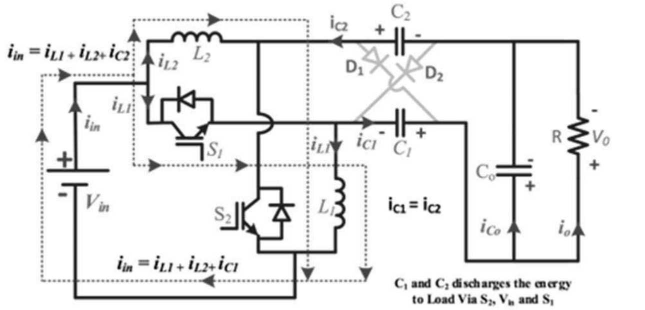

Fig. 3. Operating mode of the proposed generation side converter during active switches are ON.

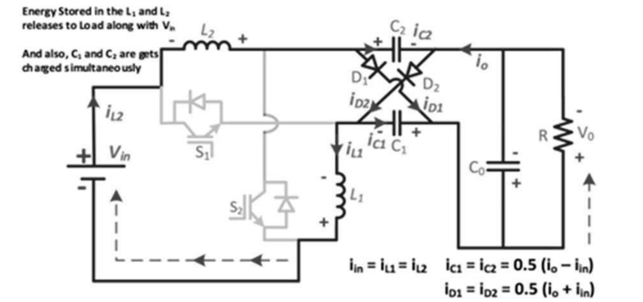

Fig. 4. Operating mode of the proposed converter while the active switches are OFF.

is by using a transformer. Fig. 2 illustrates the proposed source-side DC converter, which operates without a transformer. This converter features two active switches with identical duty cycles, along with two passive switches, two series-connected inductors, and capacitors connected in a diagonal configuration. The MPPT algorithm controls the gating signals of both active switches. The proposed source-side converter aims to reduce the number of active switches and passive components while maximizing the voltage on the DC link inverter side, with minimal switching stress. When the active switches are in the on state, the switched inductors and capacitors are charged, and when in the off state, they are discharged. The paper introduces the diagonal diode capacitor cell, which achieves maximum gain at lower duty ratios. When both diodes are turned on, the capacitors can be charged simultaneously. When diodes are blocked, the capacitor voltage can be connected in series to obtain a maximum voltage across the DC link.

This converter achieves maximum voltage gain, and its function has been thoroughly explained through mathematical analysis.

The following section analyzes the operating modes of the proposed DC converter configuration.

Mode 1: In Mode 1, the active switches are turned on by the MPPT controller, as illustrated in Fig. 3. The switched inductors are charged when the active switches are ON until they reach their maximum current. Additionally, capacitors C1 and C2 are connected in series to discharge the energy from the previous cycle. The energy is lost because of the blocking capabilities of diodes D1 and D2. The voltage relation during this period is expressed in (1):

$$V_O = V_{in} + 2V_{co} \tag{1}$$

This derivation demonstrates that the output capacitor voltage determines the DC link voltage (V_{co}), output voltage (V_O), and input voltage (V_{in}) represent the converter.

Mode 2: In this mode, the active switches are turned off, and the inductors charge the parallel capacitors through the diodes (D1 and D2). The current direction of this mode for the load is shown in Fig. 4. During this period, the relationship between voltage levels across the inductors (V_{L1}, V_{L2}) is described regarding duty cycle (d) by (2):

$$V_{L1} = V_{L2} = \frac{V_{in} - V_C}{2} \tag{2}$$

The instantaneous voltage of the inductor is derived in (3):

$$(V_{in} + 2V_c - V_O)d + (V_C - V_O)(1 - d) = 0 \tag{3}$$

From (1) - (3), the resulting voltage across the capacitor (V_C) can be determined as (4):

$$V_C = \left(\frac{V_O + V_{in}d}{1 + d}\right) \tag{4}$$

Using (1) to (4), the voltage gain (M_{CCM}) is achieved (5) for the developed converter.

$$M_{CCM} = \left(\frac{V_O}{V_{in}}\right) = \frac{1 + 3d}{1 - d} \tag{5}$$

B. Device Stress Analysis

Based on the theoretical analysis, the voltage and current expressions for the devices used in the proposed converter can be derived from the basic power expression, and the output current (I_O) can be obtained as:

$$I_O = \left(\frac{V_O + V_{in}d}{1 + d}\right) I_{in} \tag{6}$$

The average current through the inductor can be obtained from the analysis, and it can be expressed as (7):

$$I_L = \frac{I_{load}}{V_{in}} \frac{1 - d}{1 + 3d} \tag{7}$$

The designer must carefully consider device selection and analyze the maximum voltage and current through components. From the operation details, the voltage across the switches (V_{SW}) has been identified and can be written as (8):

$$V_{SW} = \left(\frac{V_{in}}{1 - d}\right) \tag{8}$$

Similarly, the RMS current flow through switches (I_{SW}) is derived and expressed as (9):

$$I_{SW} = \frac{2P_{load}\sqrt{d}}{V_{in}\,(1 + 3d)} \tag{9}$$

The voltage that appears across the diodes (V_D) during blocking states, the optimal voltage rating of the diodes should be identified. It is observed from theoretical waveforms and expressed as (10):

$$V_D = \frac{2V_{in}}{1 - d} \tag{10}$$

TABLE I
COMPARATIVE STUDY WITH DIFFERENT CONVERTERS

Converters in literature	Number of Components	Power Level (W)	Switching frequency (kHz)	Power loss (W)	Efficiency in %	Device Stress (Switch)	Device Stress (Diode)	Gain (M_{CCM})
Proposed high-gain DC-DC converter	2S, 2D, 2C, 2I	2000	25	50	97.5	$\frac{M_{CCM}}{1+3D}$	–	$\frac{1+3D}{1-D}$
Switched Hybrid converter [30]	2S, 7D, 1C, 4I	1800	20	90	95	$\frac{M_{CCM}+1}{2}$	$M_{CCM}+1$	$\frac{1+3D}{1-D}$
Transformerless high gain III [4]	2S, 3D, 3C, 2I	400	40	24	94	$\frac{M_{CCM}-1}{2}$	$M_{CCM}-1$	$\frac{3-D}{1-D}$
Hybrid converter [31]	1S, 4D, 4C, 1L	300	20	15	95	$\frac{M_{CCM}-1}{2}$	–	$\frac{3-D}{1-D}$
Input parallel and output series [28]	2S, 3D, 3C, 2L	1000	20	60	94	$\frac{M_{CCM}-1}{2}$	$\frac{M_{CCM}-1}{2}$	$\frac{2}{1-D}$
Switched capacitor boost [29]	2S, 3D, 3C, 1L	250	20	25	90	$\frac{M_{CCM}}{2}$	$\frac{M_{CCM}}{2}$	$\frac{2}{1-D}$
Switched inductor boost [36]	1S, 1D, 1C, 2L	500	20	30	94	M_{CCM}	M_{CCM}	$\frac{1+D}{1-D}$

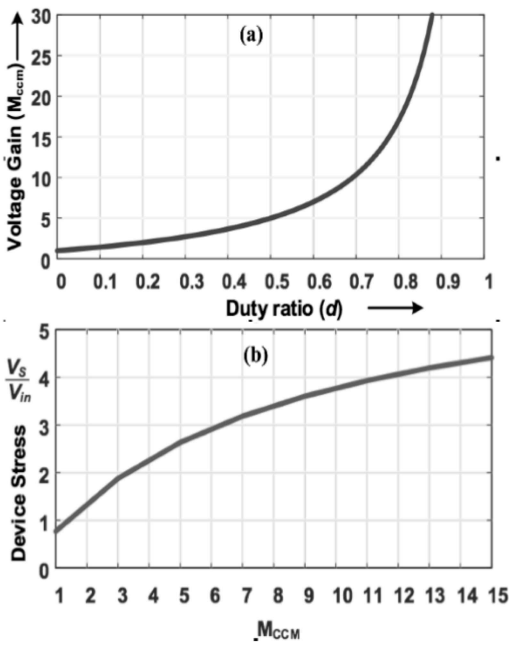

Fig. 5. Performance graph plots (a) Voltage gain and duty cycle ratio, (b) Device stress versus voltage gain.

Similarly, the current through the diode (I_{Davg}) is also analyzed from the theoretical operation and can be expressed in terms of load power (P_{load}) as (11):

$$I_{Davg} = \frac{P_{load}\,(1-d)}{V_{in}\,(1+3d)} \tag{11}$$

Device switching stress can be calculated from (8) to (11) during the converter's operation, and the converter's performance is illustrated in Fig. 5.

Table I show that our proposed converter offers a significantly higher voltage gain compared to recently developed converters while utilizing few components. This table

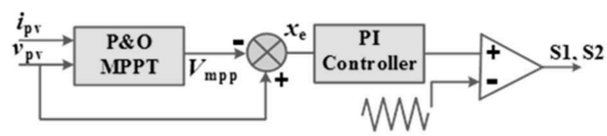

Fig. 6. Generating gating signals to the active switches of the converter.

includes various parameters, such as power losses, efficiency, device stress, and voltage gain. Additionally, the proposed generation side converter's power loss analysis and efficiency have been calculated and compared with those of the existing DC-DC converter, considering the maximum power ratings used in the system. It is inferred that the proposed generation-side converter has lower power loss and higher efficiency because of the selected switching frequency and reduced number of switches. To achieve a similar voltage gain, more than ten components, including switches (S), diodes (D), inductors (L), and capacitors (C), are required. The variation in gain values regarding duty ratios (D) is shown in Fig. 5(a), while Fig. 5(b) displays the voltage stress of the switch for various gain values.

The proposed converter achieves maximum voltage gain with fewer devices than conventional converters. Based on the switching and diode stress analysis, the proposed converter has less stress than other converters, as presented in Table I. After conducting a detailed comparative analysis, we found that the proposed converter is the most promisingsolution for improving voltage gain with minimal duty ratios.

The proposed high-gain converter maintains a constant DC link voltage by utilizing an MPPT controller and battery storage system, even during variations in irradiance. The instantaneous voltage and the current of the PV panel are measured and sent to MPPT controller to compare with

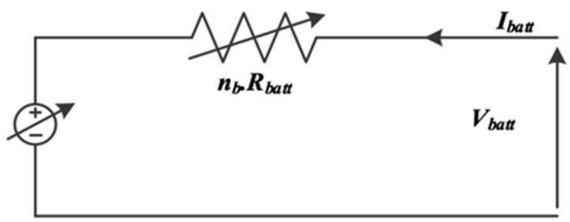

Fig. 7. Equivalent electric circuit of battery.

the maximum power point voltage (V_{mpp}), and the error signals are generated from the PI controller.

The error signals are compared with actual signals, and the generated gating pulses are applied to the active switches of the proposed converter (Fig. 6).

The DC link voltage (V_{DC}) or the output voltage of the converter can be expressed as (12):

$$V_{DC} = \frac{V_{PV}(1+3D)}{1-D} \tag{12}$$

The conditions to generate the gating signals to the active switches have been derived as (13):

$$S_1, S_2 = \{ON; V_{PV} \neq V_{mpp} OFF; V_{PV} = V_{mpp}\} \tag{13}$$

C. Power Loss Calculation

The analysis of the battery storage unit simulation is illustrated in Fig. 7.

The amount of energy a battery can store is primarily determined by its charging current. However, the voltage changes because of the SoC. The relationship between the terminal voltage (V_{batt}), battery cell, internal resistance, and current, and open circuit battery voltage (E_{batt}) is expressed in (14):

$$V_{batt} = n_b \times E_{batt} \pm n_b \times R_{batt} \times I_{batt} \tag{14}$$

where n_b is the number of cells connected in series, R_{batt} is the internal resistance of the battery, I_{batt} is the battery current. The capacity of the battery C_{batt} depends on the temperature accumulated inside the battery (T), and the maximum charge rating (C_{rated}), and is expressed in (15):

$$C_{batt} = C_{rated} \times \frac{1.67\times (1 + 0.005 \times \Delta T)}{\left(\frac{I}{I_{10}}\right)^{0.9}} \tag{15}$$

The SoC is inversely proportional to the depth of discharge, and it can be expressed as (16):

$$SoC = 1 - \frac{Q}{Q_{batt}} \tag{16}$$

where Q is the cumulative charge, and Q_{batt} is the cumulative charge capacity.

III. Implementation of DC Link Voltage Control and Energy Management System

To ensure proper coordination among the PV generator, battery storage, high-gain DC-DC converter, and transformerless inverter, a real-time power management strategy has been implemented in Fig. 8. The system continuously monitors input power, load demand, and battery SoC to make dynamic control decisions. During surplus generation, the battery charges while maintaining regulated DC link voltage

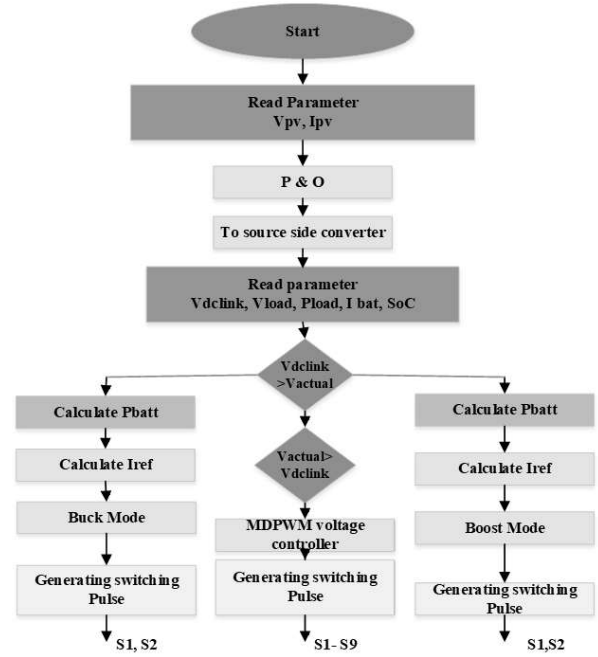

Fig. 8. Flowchart for energy management system.

In deficit scenarios, the battery discharges to supply the load through bidirectional power flow. The MPPT controller ensures maximum energy extraction by controlling the converter duty ratio through a PI loop. A logical control flow sequence ensures smooth transitions between modes, preserving voltage stability and reducing component stress. This coordinated subsystem interaction enables efficient energy balancing across variable solar and load conditions.

The existing conventional approach measures the power deviation from the load and generation side in a few cycles. This variation is carried out throughout the day. In our algorithm, the DC link voltage of the inverter is measured instantaneously based on deviations from the PV panel and load sides. The source power and the inverter DC link voltage decrease as the load power increases. During this period, the proposed converter operates in a boost configuration, maintaining a constant DC link voltage.

In the existing methods, power balancing approach algorithms such as Pulse Phase Shift, PWM pulse dual phase shift, Modified Pulse Phase Shift, and Zero Voltage Switching are utilized to measure power variances between the load and generation sides. However, these approaches result in a time delay in maintaining the DC link voltage. Additionally, these algorithms cause high circulating current during heavy load conditions [23], [24]. In the proposed algorithm, the measured variations between the DC link voltage and load voltage generate instant gating signals for the proposed converter, enabling buck and boost mode operations with the aid of a closed-loop controller. The modified discontinuous PWM technique is used for the H-7 inverter configuration (load-side converter).

A. DC Link Voltage Control Based on Reference Current Generator

The reference to the current generation of the converter is crucial to obtaining the optimum power level and to ensuring the converter's.

Bidirectional current flow capability in the charging and discharging modes. The battery reference current (i_{bat_ref}) has been derived from the reference DC link voltage (V_{dclink}), actual DC link voltage (V_{dclink_act}), battery reference power (P_{bat_ref}) and actual battery voltage (V_{bat}) in (17):

$$i_{bat\_ref} = \left(1 + \frac{V_{dclink} - V_{dclink\_act}}{V_{dclink}}\right)\frac{P_{bat\_ref}}{V_{bat}} \tag{17}$$

where the battery reference power (P_{bat_ref}) calculated using PV power (P_{PV}) and load power (P_{load}) in (18),

$$P_{bat\_ref} = P_{PV} - P_{load} \tag{18}$$

and the P_{load} is estimated from load voltage (V_{load}) and load current (i_{load}) in (19):

$$P_{load} = V_{load} \times i_{load} \tag{19}$$

B. Energy Management Systems

Despite load variations, the DC-side inverter voltage should be maintained at a constant level for optimal performance. The proposed EMS enable load variations through a battery storage system in two modes of operation. According to load power consumption, the EMS is categorized as follows:

$$Power\ stored\ in\ the\ battery$$
$$(P_{PV} > P_{load}\ and\ V_{dclink} > V_{dclink\_act})$$

When the power produced by the PV system surpasses the power needed by the load, the DC link voltage increases beyond its steady-state value. If the DC link voltage exceeds 90% of its rated value, the MPPT controller regulates the current flow from the battery to the DC link. The DC link power (P_{DC}) can be determined using (20):

$$P_{PV} - P_{bat} = P_{DC} + P_{loss} \tag{20}$$

During power imbalance conditions, a difference between solar PV generation and battery power, which can be calculated using (20). However, in practical consideration, the total losses of the system P_{loss} are also included in (20). The voltage gain of the converter is calculated based on the error signals provided to the PI controller. The switches are controlled dynamically by MDPWM gate pulses based on the PI response. The system responses are based on the error function and proportional plus integral gain values. Based on the error feedback, the system gets tuned automatically to improve the system's response, which can be expressed as (21):

$$r = K_p e(t) + K_I \int e(t)dt \tag{21}$$

The proportional and integral gains of K_P and K_I primarily determine the system's response. This calculated signal is used to intersect the carrier signal, generating the required MDPWM signal for the proposed DC-DC converter. Here, the battery operates in charging mode.

$$Power\ dissipated\ from\ the\ battery$$
$$(P_{PV} < P_{load} and V_{dclink} < V_{dclink\_act})$$

During this period, the DC link voltage of the inverter does not meet the load demand. The proposed converter operates as a boost converter to maintain the inverter's constant

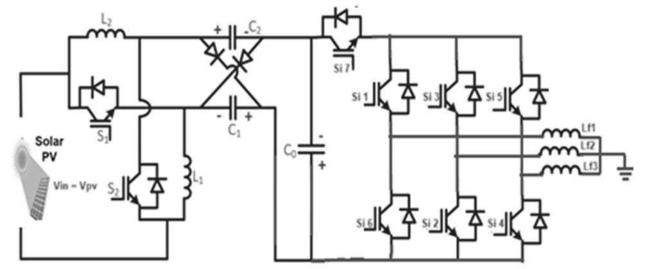

Fig. 9. Proposed DC-DC converter with H-7 Transformerless Inverter.

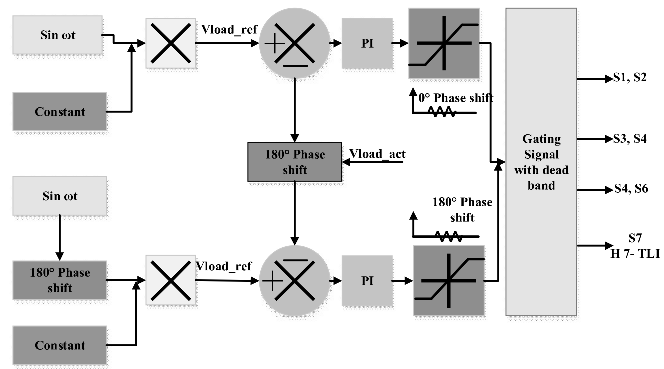

Fig. 10. Functional block diagram of MDPWM controller.

DC link voltage. For the boost mode operation of the converter, the duty cycle must be greater than the value given in (22):

$$d_{min} = 1 - \frac{V_{bat\_ref}}{V_{dc\_ref}} \tag{22}$$

During the minimum battery voltage range, the converter must be able to operate under minimum duty ratios. The practical minimum duty ratio (d_{min} The efficiency of the DC-DC converter is 0.2. Below that, the inductor core may become saturated, which can be estimated using (22). The DPWM switching pulse of the proposed converter is expressed as (23):

$$Pulses = \{S_3 ON; P_{PV} > P_{load}; V_{dclink} < V_{dclink\_act} S_4 OFF; \\ P_{PV} < P_{load}; V_{dclink} > V_{dclink\_act}\} \tag{23}$$

C. Transformerless Inverter Controller

The H-7 transformerless inverter configuration with the proposed DC-DC converter is given in Fig. 9.

The transformerless inverter helps maintain the load voltage at the reference value while operating with a limited switching frequency. The complete functional block diagram of the MDPWM controller is presented in Fig. 10. The MDPWM controller for the H-7 transformerless inverter provides improved performance for both grid-connected and standalone systems. It operates in voltage-controlled mode, and to achieve a sinusoidal pattern, a constant value is multiplied by a sine wave to adjust the reference point. The inverted output signal is related to the actual load signal, generating an error signal.

The PI controller adjusts the error signal, resulting in a limited output. The PI output is magnified proportionally and

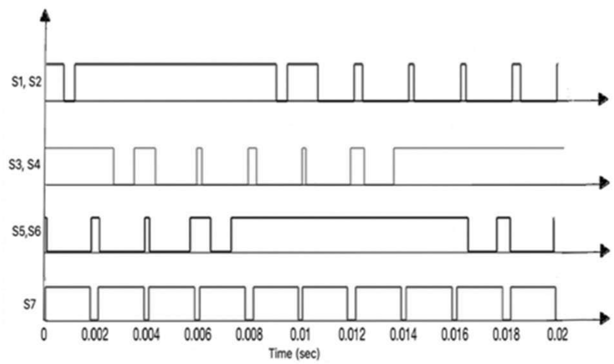

Fig. 11. MDPWM signal for H-7 Transformerless Inverter.

integrally, but is limited to assigned positive and negative limits. Finally, the gating signal is obtained after comparing it with the fixed triangular signal. Additionally, a 180° out-of-phase reference pattern is generated to get the desired gating signal. The final gating signal is the MDPWM pattern, which helps to yield a sinusoidal output voltage. Because of a mismatch in the gating pattern, the upper and lower switches frequently form a short-circuit path. The controller has a fixed dead time to prevent short-circuit current flow between upper and lower switches. The MDPWM reference signal has been given in (24)

$$V_{ar} = V_{gr} + V_o = msin\,(\omega t) + V_o \tag{24a}$$

$$V_{br} = V_{gy} + V_o = msin\,(\omega t - 2\pi/3) + V_o \tag{24b}$$

$$V_{cr} = V_{gb} + V_o = msin\,(\omega t + 2\pi/3) + V_o \tag{24c}$$

$V_{ar}, V_{br,} V_{cr}$ The reference signal is applied to the proposed MDPWM technique. V_{gr}, V_{gy}, *and* V_{gb} are the ideal sinusoidal reference signals. V_o is zero sequence.

$$V_o = \left[sign\,(V_{max})\right](V_{DC}/2 - V_{max}) \tag{25}$$

In (25), V_{max} is the ideal sinusoidal reference with maximum magnitude. This signal is compared with a triangular carrier signal to generate a PWM pulse.

The generated pulses for the transformerless inverter configuration are shown in Fig. 11.

D. Efficiency Analysis

The efficiency of the proposed converter has been determined by calculating the power losses in the switching devices. The power losses in the IGBT (P_{IGBT}) and diode (P_{Diode}) have been expressed in (26) and (27).

$$P_{IGBT} = IGBT_{cond} + IGBT_{sw} \tag{26}$$

$$P_{Diode} = Diode_{cond} + Diode_{sw} \tag{27}$$

The power losses of the IGBT and the diode are calculated with conduction ($IGBT_{cond}, Diode_{cond}$) and switching losses ($IGBT_{sw}, Diode_{sw}$)*o* of the devices. The power losses of the IGBT have been calculated using (28) and (29).

$$IGBT_{cond} = V_{ce(sat)\times} I_c \tag{28}$$

$$IGBT_{sw} = E_{ON} \times fsw \times \frac{V_{cc}}{V_{cc_{datasheet}}} + E_{OFF} \times fsw \times \frac{V_{cc}}{V_{cc_{datasheet}}} \tag{29}$$

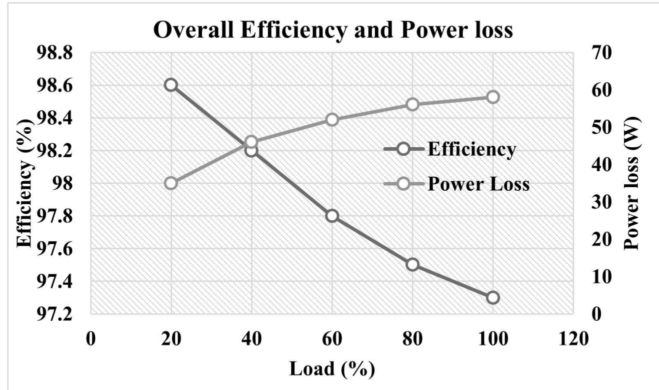

Fig. 12. Overall efficiency and power loss of the proposed system.

E_{ON} and E_{OFF} Represent the turn-on and turn-off losses of the IGBT. V_{cc} denotes the actual DC bus voltage, whereas $V_{cc_{datasheet}}$ refers to the DC bus voltage listed on the datasheet. Various switching frequencies (fsw) are used for both the DC-DC converter and the inverter. The diode conduction losses and switching losses have been expressed in (30) and (31)

$$Diode_{cond} = V_F \times I_F \tag{30}$$

$$Diode_{sw} = \frac{1}{8} \times T_{rr} \times V_{rr} \times V_R \times f\,sw \tag{31}$$

The forward voltage (V_F) and forward current (I_F) of the diode are used to calculate diode conduction losses. The reverse recovery time (T_{rr}), reverse recovery voltage (V_{rr}), and reverse blocking voltage (VR) have been considered calculating the switching loss of the diode.

$$P_{sw(DC-DC)} = P_{LI} = P_{IGBT} + P_{Diode} \tag{32}$$

From the expression (32), the switching losses of the DC-DC converter ($P_{sw(DC-DC)}$) and transformerless inverter (P_{LI}) has been calculated. R_h is the load resistance of the converter.

$$\eta_{DC-DC} = \frac{P_o}{P_{in}} = \left(\frac{\frac{V_o^2}{R_h} - P_{sw(DC-DC)}}{\frac{V_{in}V_o(1+3d)}{R_h(1-d)}}\right) \tag{33}$$

The efficiency of the DC-DC converter has been given in (33)

$$\eta_{PL} = \eta_{DC-DC} - P_{LI} \tag{34}$$

The overall efficiency (η_{PL}) of the system is calculated to be 97.7% using expression (34). This was achieved with a smaller number of active devices in the H-7 transformerless configuration compared to other transformerless inverter configurations.

Fig. 12 illustrates the overall power loss and efficiency of the proposed system under various load conditions. This has been calculated using the equation form. The proposed system achieves maximum efficiency at full capacity with minimal power loss. Compared to existing non-isolated high-gain converters such as the switched hybrid converter [30], transformerless high-gain III [4], and switched capacitor/inductor converters [28], [29], [36], the proposed topology achieves a higher efficiency of 97.7% with reduced power losses. These existing configurations typically report efficiencies in the 90-95% range with higher device stress and larger component counts (as summarized in Table I).

TABLE II
SIMULATION PARAMETERS

Parameter	Values
Solar PV module capacity	5 kWp
Inductance L1 and L2	1 mH
Capacitance C1 and C2	100 uF
H-7 filter inductor	15 mH
H-7 filter capacitor	1200 uF
bidirectional converter inductor	0.5 mH
generation-side converter switching frequency	25 kHz
H-7 inverter switching frequency	15 kHz
Nominal battery voltage	48 V
Nominal battery capacity	500 Ah

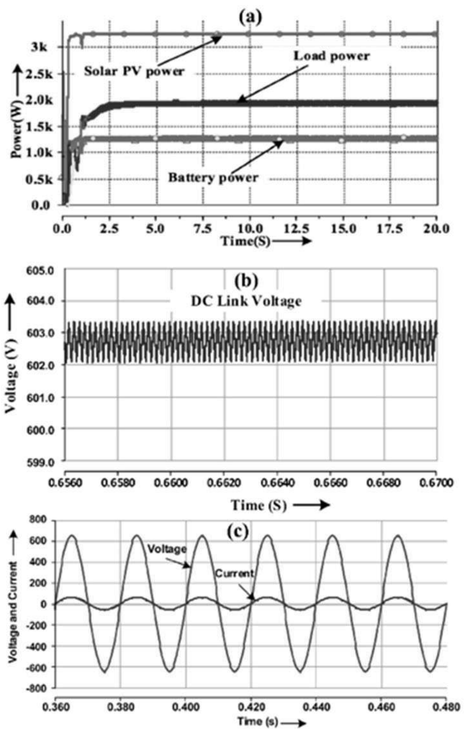

Fig. 13. Results at $P_{PV} > P_{load}$: (a) steady state power analysis of solar PV, battery, and load; (b) DC link voltage deviation <2% (c) H-7 inverter output voltage and current.

IV. Simulation Results and Discussion

The whole system (generation side and load side converter) simulation has been carried out and tested using MATLAB/Simulink software. The simulated parameters of both side converters are given in Table II.

Load and battery power are measured at a standard irradiance of 800 W/m^2 to evaluate the power management system. We present the power graph results to analyze the effectiveness of our energy management strategy. Under full solar irradiance (800 W/m^2) and a low load of 500 W, the PV system generates surplus power. The energy management strategy effectively diverts excess power to the battery. Under these conditions, the power at the load side, solar PV side, and battery side is measured, as shown in Fig. 13(a). Fig. 13(b) illustrates the

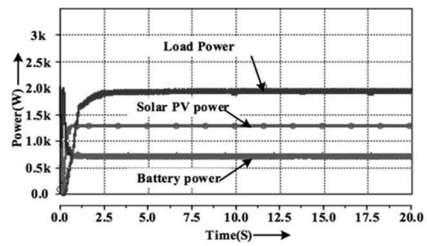

Fig. 14. Steady-state condition when $P_{PV} > P_{load}$: battery discharge ≈ 1-2 kW; DC link voltage deviation <2%.

fluctuations in the DC link, which are minimal during steady-state conditions. The DC link voltage remained well regulated, with observed fluctuation <2%. The MPPT maintained its tracking accuracy throughout the entire process. This validates the system's ability to support storage-first strategies during light load conditions. Here, the battery operates in charging mode ($P_{bat} < 0$), with SoC increasing steadily. The DC link voltage is regulated within ±2% of the 600 V reference during steady state, while transient overshoots under irradiance changes remain below 5%. When the PV power generated is less than the load power, the DC link voltage will drop from the steady-state value. During this condition, the battery supplies power to the load. Additionally, the battery power direction is reversed, with a positive magnitude, as shown in the simulation results. With MDPWM control, pure sinusoidal voltage and equivalent current waveforms can be generated at the load side through an inverter. This has been mentioned in Fig. 13(c). Fig. 14 shows the simulation analysis performed to verify the proposed system's performance when the load power requirement exceeds the solar PV power. DC-link-centric power management has also been demonstrated in prior studies [45], further confirming the effectiveness of the adopted strategy.

The PV system was subjected to variable load profiles ranging from 1.2 kW to 2.5 kW in increments of 400 W, while irradiance was maintained at a constant level of 800 W/m^2. The DC-DC converter dynamically adjusted duty ratios to keep the DC link voltage within ±5% of the nominal value. The system transitioned seamlessly between battery discharge and power-sharing modes. This case emphasizes the controller's responsiveness to user-side demand changes. Here, the battery supplies the deficit in discharging mode ($P_{bat} > 0$), leading to a reduction in SoC. The DC link voltage experiences a drop during load transients but is restored within ±5% and settles to within ±2% of 600 V once steady state is reached. When PV generation closely matches load demand, the battery is in an idle or standby state. Here, the DC link voltage is maintained.

Very close to its reference, typically within ±1% of 600 V, as no significant power imbalance needs to be compensated. The simulation results are measured under dynamic conditions. Power measurements were performed to evaluate the controller's performance during sudden changes in solar irradiation (Fig. 15). After 10 seconds, the solar irradiation decreased from 800 W/m^2 to 400 W/m^2. Therefore, the solar PV generation becomes 1.3 kW. When the load conditions are the same, the battery gets discharged to compensate for the surplus power of 700 W required by the load. This is

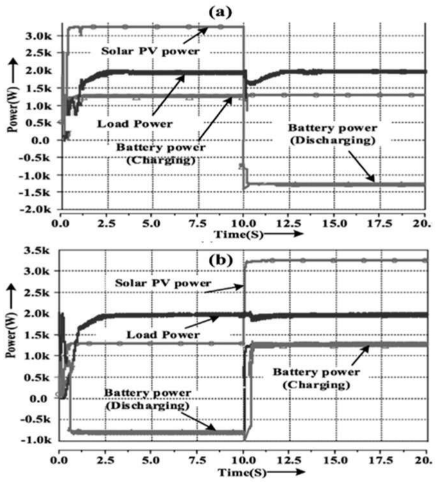

Fig. 15. Power analysis at dynamic solar irradiations: (a) irradiance drop from 800 W/m^2 to 400 W/m^2, battery discharge ≈ 0.7 kW, DC link deviation within ±5%; (b) irradiance recovery, battery charging ≈ 0.6 kW, DC link deviation within ±5%.

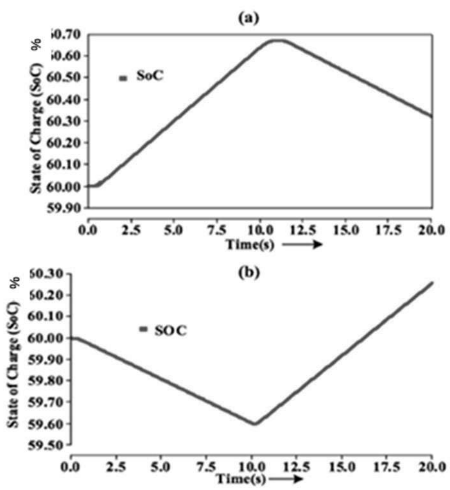

Fig. 16. Battery state-of-charge analysis (a) sudden decrease in solar irradiance after 10s (b) sudden increase in solar irradiance after 10s.

also clearly illustrated in Fig. 15(a). Similarly, when solar irradiation increases from 400 W/m^2 to 800 W/m^2 because of environmental factors, the measured results are presented in Fig. 15(b).

Fig. 16 (a). and (b) show the battery SoC graph under the same conditions. Thus, the dynamic results validate the implementation of the energy management control strategy. The DC link voltage plays a crucial role in maintaining the inverter's stability and enabling proper power transfer between the solar PV, battery storage, and load. During regular operation, the controller maintains the DC link voltage at approximately 600 V, serving as the regulated reference point. A maximum allowable deviation of ±5% from the setpoint is tolerated under transient conditions such as load surges or irradiance dips. The proposed control algorithm ensures that any deviation beyond this margin is corrected in real time by adjusting the converter duty ratio and switching between charge/discharge battery modes. With a 1.8 kW load and solar input at 600 W/m^2, the battery initially discharged to

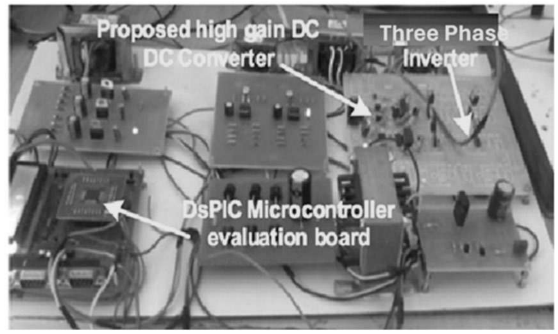

Fig. 17. Experimental setup.

compensate for the deficit. Once the SoC reached 25%, the controller gradually reduced the discharge rate, prioritizing system stability over continuous discharge.

This illustrates that intelligent SoC-aware operation prevents deep discharge and extends battery life. Additionally, the system exhibits a response time of less than 1.5 ms, confirming its real-time adaptability.

V. Experimental Results and Analysis

The proposed energy management strategy was validated (Fig. 17) through an experimental setup; this section presents the results. The parameter values chosen for the experimental test are the same as the simulation result. The dsPIC microcontroller board generates the necessary PWM signals to perform the experimental work. The IRFP260N device serves as a power switch, while the MUR3060 fast-recovery diode is utilized in the DC-DC converter stage. This proposed system was implemented and evaluated on a low-cost hardware platform. The switching devices used were IRFP260N MOSFETs and MUR3060 ultrafast diodes, selected for their voltage and current ratings, which are suitable for mid-power PV systems.

The controller was a dsPIC microcontroller, which executed the MPPT algorithm and generated gating pulses. A programmable DC power supply was used to emulate varying solar irradiance conditions. Load variations were introduced using a digitally controlled resistive load bank. System currents and voltages were monitored in real-time using Hall-effect-based sensors (ACS712) and visualized using a 4-channel digital oscilloscope. Additional measurements were logged using a USB data acquisition card. Sampling was done at 10 kHz to ensure sufficient control loop responsiveness. A copper strip board is used at the bottom of the PCB circuit to withstand the current rating.

The results of the MPPT operation are displayed in Fig. 18, which includes the gating signal, DC link voltage, and solar PV voltage at various levels of solar irradiation. It is evident from Figs. 18(a) and 18(b) that the DC link voltage remains stable to balance power, even when power levels fluctuate, which is attributed to the proposed energy management strategy.

To verify the operation of the solar PV fed MDPWM inverter, a zoomed view of the output load voltage and reference voltage is shown in Fig. 19 (a). Throughout the day, the load voltage closely follows the reference voltage. Also, the inductor is discharged during the off state

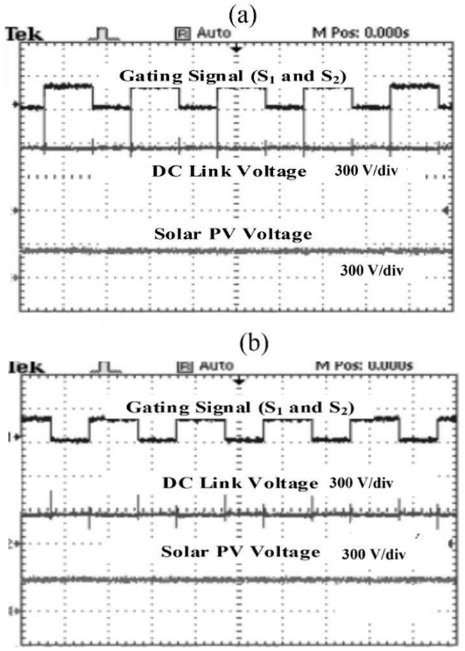

Fig. 18. Gating signal, DC link voltage, and solar PV voltage for solar irradiation **(a)** 800 W/m^2 (b) 400 W/m^2.

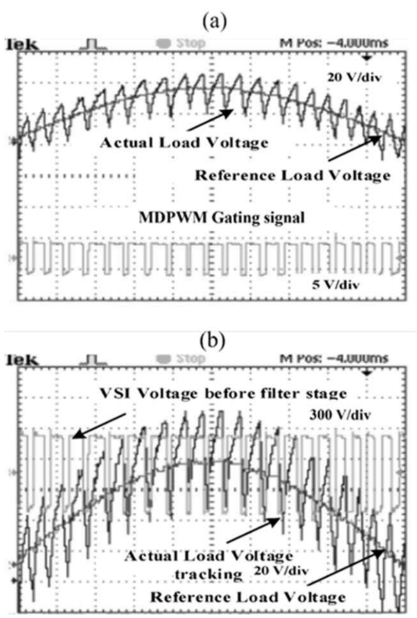

Fig. 19. Zoomed view of tracking performance (a) gating signal, reference, and actual load voltage; (b) VSI output, reference, and load voltage signal.

and charged during the on state at the output side of the proposed inverter. Additionally, as mentioned earlier, the controller generates a gating signal, as shown in Fig. 19(b), and presents the experimental results of the voltage produced by the VSI under MDPWM strategies in a zoomed view. Furthermore, Fig. 19(b) displays tracking performance and illustrates the relationship between changes in inductor current and voltage. The experimental results for the load voltage, load current, and the voltage across the transformerless inverter are presented in Figs. 20(a) and 20(b). The voltage profile exhibits a slight ripple because of the

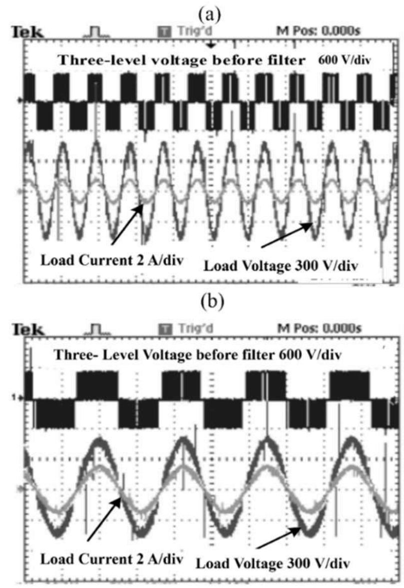

Fig. 20. Experimental VSI output, reference voltage, and load voltage (a) Normal view (b) Zoomed view.

load's behavior. These experimental findings validate that the proposed optimal power control strategy is well-suited for solar PV fed hybrid systems.

The theoretical and simulation results indicate that the overall efficiency of the proposed system is 95.7%. The experimental efficiency is 95.3%, exhibiting minimal variations from theoretical and simulated values. The validation of the proposed system was conducted on a laboratory prototype rated up to 2.5 kW, successfully demonstrating stable DC link regulation, a fast transient response, and high efficiency under varying load and irradiance conditions. While this power rating is adequate for laboratory-scale verification, larger-scale PV systems typically operate at higher capacities. Extending the design and validation to higher power levels and grid-connected operation will therefore be an important direction for future work. The present validation did not include thermal stress analysis of semiconductor devices or long-term reliability studies such as battery degradation. These aspects, while outside the scope of the current laboratory-scale work, are critical for practical deployment and will be addressed in future studies.

VI. Conclusion

The proposed method offers several technical advantages: high voltage gains with low duty ratio operation, real-time power flow coordination, fewer power components, and lower switching losses. The design integrates inverter control and MPPT in a unified scheme, reducing computational and hardware complexity. However, the present system has been validated only up to 2.5 kW and does not yet incorporate grid synchronization or fault-tolerant features. Its reliance on silicon devices also constrains thermal performance and switching frequency, while long-term battery degradation and predictive power scheduling remain unaddressed. To address these gaps, future work will focus on extending the design for higher power ratings and grid-tied operation, integrating wide-bandgap devices such as SiC and GaN for higher efficiency and compactness, embedding advanced fault detection, predictive diagnostics, and machine learning based forecasting, as well as incorporating thermal modeling of components and battery degradation analysis to enhance system reliability and lifecycle performance.

References

[1] F. Belhachat and C. Larbes, "Modeling, analysis and comparison of solar photovoltaic array configurations under partial shading conditions," *Sol. Energy*, vol. 120, pp. 399–418, Oct. 2015, doi: 10.1016/j.solener.2015.07.039.

[2] P. Pandian, P. W. David, P. Murugesan, and P. K. Balachandran, "A selective cross-tied array configuration technique for partial shaded solar PV system," *Electr. Eng.*, vol. 106, no. 4, pp. 4059–4078, Jan. 2024, doi: 10.1007/s00202-023-02209-3.

[3] X. Liu, S. Kent Hoekman, C. Robbins, and P. Ross, "Lifecycle climate impacts and economic performance of commercial-scale solar PV systems: A study of PV systems at Nevada's desert research institute (DRI)," *Sol. Energy*, vol. 119, pp. 561–572, Sep. 2015, doi: 10.1016/j.solener.2015.05.001.

[4] M. Zaid et al., "A transformerless high gain DC–DC boost converter with reduced voltage stress," *Int. Trans. Electr. Energy Syst.*, vol. 31, no. 5, pp. 1–17, May 2021, doi: 10.1002/2050-7038.12877.

[5] B. Xu, H. Zhao, H. Cao, S. Garg, and M. Alrashoud, "Long-term energy management empowered hierarchical federated learning for smart consumer electronics," *IEEE Trans. Consum. Electron.*, vol. 70, no. 1, pp. 1155–1166, Feb. 2024, doi: 10.1109/TCE.2024.3355058.

[6] J. Yao, Q. Mao, Y. Xie, and S. Qiao, "Energy-load collaborative optimization method based on fuzzy-SM-GA in consumer electronics," *IEEE Trans. Consum. Electron.*, vol. 71, no. 2, pp. 7024–7031, May 2025, doi: 10.1109/TCE.2025.3552100.

[7] S. Ramasamy, Z. Ahmad, Y. Bindu, and J. R. Torres, "Simulation based analysis of transformerless photovoltaic inverter topologies for reactive power handling capability," in *Proc. 2nd Int. Conf. Inventive Res. Comput. Appl. (ICIRCA)*. India: IEEE, Jul. 2020, pp. 1028–1034, doi: 10.1109/ICIRCA48905.2020.9182839.

[8] E. Bianconi et al., "Perturb and observe MPPT algorithm with a current controller based on the sliding mode," *Int. J. Electr. Power Energy Syst.*, vol. 44, no. 1, pp. 346–356, Jan. 2013, doi: 10.1016/j.ijepes.2012.07.046.

[9] M. E. Şahin, "A photovoltaic powered electrolysis converter system with maximum power point tracking control," *Int. J. Hydrogen Energy*, vol. 45, no. 16, pp. 9293–9304, Mar. 2020, doi: 10.1016/j.ijhydene.2020.01.162.

[10] N. Ramachandran, S. Murugan, C. Vinayagam, and P. K. Balachandran, "Real-time implementation of a seven-level multilevel DC link inverter for solar PV system during partial shading," *Electr. Power Compon. Syst.*, vol. 51, no. 18, pp. 2125–2134, Nov. 2023, doi: 10.1080/15325008.2023.2207177.

[11] D. Barater, E. Lorenzani, C. Concari, G. Franceschini, and G. Buticchi, "Recent advances in single-phase transformerless photovoltaic inverters," *IET Renew. Power Gener.*, vol. 10, no. 2, pp. 260–273, Feb. 2016, doi: 10.1049/iet-rpg.2015.0101.

[12] S. Ramasamy, R. Baccoli, S. Meo, G. Gatto, and A. Kumar, "Neutral point clamped non-isolated three phase grid-integrated PV inverter topologies for leakage current reduction," *Int. Rev. Electr. Eng. (IREE)*, vol. 18, no. 2, p. 88, Apr. 2023, doi: 10.15866/IREE.V18i2.23629.

[13] M. Islam and S. Mekhilef, "Efficient transformerless MOSFET inverter for a grid-tied photovoltaic system," *IEEE Trans. Power Electron.*, vol. 31, no. 9, pp. 6305–6316, Sep. 2016, doi: 10.1109/TPEL.2015.2501022.

[14] H. Mahmood, D. Michaelson, and J. Jiang, "A power management strategy for PV/battery hybrid systems in islanded microgrids," *IEEE J. Emerg. Sel. Topics Power Electron.*, vol. 2, no. 4, pp. 870–882, Dec. 2014, doi: 10.1109/JESTPE.2014.2334051.

[15] S. S. Somalinga and K. R. Santha, "Non-isolated enhanced gain of DC–DC converter for DC micro-grid applications," *Int. Trans. Electr. Energy Syst.*, vol. 30, no. 12, pp. 1–20, Dec. 2020, doi: 10.1002/2050-7038.12625.

[16] C. P. Ragasudha and S. Hemamalini, "Performance analysis of a high gain bidirectional DC–DC converter fed drive for an electric vehicle with battery charging capability during braking," *IEEE Access*, vol. 12, pp. 14499–14511, 2024, doi: 10.1109/ACCESS.2024.3357726.

[17] F. Khan, M. Zaid, A. Tariq, and M. M. A. Khan, "A new non-isolated high-gain DC–DC converter for the PV application," *E-Prime-Adv. Electr. Eng., Electron. Energy*, vol. 5, Sep. 2023, Art. no. 100198, doi: 10.1016/j.prime.2023.100198.

[18] L. Kong, J. Yu, and G. Cai, "Modeling, control and simulation of a photovoltaic /hydrogen/ supercapacitor hybrid power generation system for grid-connected applications," *Int. J. Hydrogen Energy*, vol. 44, no. 46, pp. 25129–25144, Sep. 2019, doi: 10.1016/j.ijhydene.2019.05.097.

[19] N. Yang, Y. Wang, Y. Zhang, and D. Yuan, "Non-intrusive load monitoring for energy management in smart grids incorporating EVs," *IEEE Trans. Consum. Electron.*, vol. 71, no. 1, pp. 1696–1706, Feb. 2025, doi: 10.1109/TCE.2024.3489580.

[20] M. Zeifman and K. Roth, "Nonintrusive appliance load monitoring: Review and outlook," *IEEE Trans. Consum. Electron.*, vol. 57, no. 1, pp. 76–84, Feb. 2011, doi: 10.1109/TCE.2011.5735484.

[21] F. Li and H. Liu, "A cascaded coupled inductor-reverse high step-up converter integrating three-winding coupled inductor and diode–capacitor technique," *IEEE Trans. Ind. Informat.*, vol. 13, no. 3, pp. 1121–1130, Jun. 2017, doi: 10.1109/TII.2016.2637371.

[22] S. Hasanpour and T. Nouri, "New coupled-inductor high-gain DC/DC converter with bipolar outputs," *IEEE Trans. Ind. Electron.*, vol. 71, no. 3, pp. 2601–2613, Mar. 2024, doi: 10.1109/TIE.2023.3270512.

[23] J. Huang, H. Han, G. Xu, X. Liu, W. Xiong, and M. Su, "Coupled-inductor-based bidirectional resonant converter with reduced component count and load-independent voltage gain," *IEEE Trans. Ind. Electron.*, vol. 71, no. 2, pp. 1559–1571, Feb. 2024, doi: 10.1109/TIE.2023.3262870.

[24] C. Pradhan, M. K. Senapati, S. G. Malla, P. K. Nayak, and T. Gjengedal, "Coordinated power management and control of standalone PV-hybrid system with modified IWO-based MPPT," *IEEE Syst. J.*, vol. 15, no. 3, pp. 3585–3596, Sep. 2021, doi: 10.1109/JSYST.2020.3020275.

[25] M. K. Senapati, O. Al Zaabi, K. Al Hosani, K. Al Jaafari, C. Pradhan, and U. R. Muduli, "Advancing electric vehicle charging ecosystems with intelligent control of DC microgrid stability," *IEEE Trans. Ind. Appl.*, vol. 60, no. 5, pp. 7264–7278, Sep. 2024, doi: 10.1109/TIA.2024.3413052.

[26] M. K. Senapati, C. Pradhan, S. Padmanaban, and O. A. Zaabi, "Photovoltaic MPPT performance adaptability to partial shading resilience and load variations with modified adaptive Jaya optimization," *IEEE Trans. Consum. Electron.*, vol. 71, no. 1, pp. 734–747, Feb. 2025, doi: 10.1109/TCE.2025.3532660.

[27] A. Alsafrani, M. Shahbazi, and A. Horsfall, "High gain DC–DC voltage lift switched-inductor multilevel boost converter for supporting grid connection of wave energy conversion," in *Proc. 11th Int. Conf. Power Electron., Mach. Drives (PEMD)*, Jun. 2022, pp. 754–758, doi: 10.1049/ICP.2022.1138.

[28] M. Jamali, S. Ghassemzadeh, and S. H. Hosseini, "A two-phase hybrid switched-inductor DC–DC converter with high voltage conversion ratio," in *Proc. 12th Power Electron., Drive Syst., Technol. Conf. (PEDSTC)*, Feb. 2021, pp. 1–7, doi: 10.1109/PEDSTC52094.2021.9405965.

[29] Q. Tian, X. Zhang, G. Zhou, H. Li, and H. Ma, "Improved dual active bridge DC–DC converter with symmetric bipolar output by utilizing a switched-capacitor circuit for bipolar DC distribution system," *IEEE Trans. Ind. Electron.*, vol. 71, no. 1, pp. 524–536, Jan. 2024, doi: 10.1109/TIE.2023.3247748.

[30] Z. Saadatizadeh, P. C. Heris, and A. Mantooth, "High-frequency three-port DC–DC converter with zero-voltage switching operation," *IEEE Trans. Ind. Electron.*, vol. 71, no. 1, pp. 537–548, Jan. 2024, doi: 10.1109/TIE.2023.3245209.

[31] A. Kumar, S. Ramasamy, M. Losito, and G. Gatto, "Comparative analysis of three phase hybrid transformerless inverters for PV applications," in *Proc. Int. Conf. Clean Electr. Power (ICCEP)*, Jun. 2023, pp. 254–259, doi: 10.1109/ICCEP57914.2023.10247435.

[32] R. Suganthi and M. Pandi, "Improved three phase H-7 transformerless inverter with DPWM to reduce leakage current using CNN based deep learning technique," *Artif. Intell. Rev.*, vol. 56, no. 2, pp. 1319–1347, Feb. 2023, doi: 10.1007/s10462-022-10187-4.

[33] P. Li, L. M. Hoi, Y. Wang, and S. K. Im, "Data augmentation with ECAPA-TDNN architecture for automatic speaker recognition," in *Proc. 12th Int. Conf. Renew. Energy Res. Appl. (ICRERA)*, Aug. 2023, pp. 414–420, doi: 10.1109/ICRERA59003.2023.10269366.

[34] Y. Wang, J. Yan, J. Wang, and Y. Geng, "A novel hybrid transfer learning approach for small-sample high-voltage circuit breaker fault diagnosis on-site," in *Proc. IEEE 5th Int. Electr. Energy Conf. (CIEEC)*, May 2022, pp. 922–927, doi: 10.1109/CIEEC54735.2022.9846507.

[35] S. Ramasamy, V. Sivasubramaniyam, G. Gatto, and A. Kumar, “DC link voltage control based energy management strategy for standalone solar PV fed hybrid system,” in *Proc. AEIT Int. Conf. Electr. Electron. Technol. Automot. (AEIT AUTOMOTIVE)*, Jul. 2023, pp. 1–6, doi: 10.23919/AEITAUTOMOTIVE58986.2023.10217257.

[36] N. Subha Lakshmi, A. K. Harini, J. Helina, T. R. Kamalashini, and M. Kaviya, “Four port DC–DC buck boost converter for hybrid renewable energy sources,” in *Proc. 3rd Int. Conf. Electron. Sustain. Commun. Syst. (ICESC)*, Aug. 2022, pp. 84–91, doi: 10.1109/ICESC54411.2022.9885297.

[37] Y. Tang, D. Fu, T. Wang, and Z. Xu, “Hybrid switched-inductor converters for high step-up conversion,” *IEEE Trans. Ind. Electron.*, vol. 62, no. 3, pp. 1480–1490, Mar. 2015, doi: 10.1109/TIE.2014.2364797.

[38] B. Wu, S. Li, Y. Liu, and K. Ma Smedley, “A new hybrid boosting converter for renewable energy applications,” *IEEE Trans. Power Electron.*, vol. 31, no. 2, pp. 1203–1215, Feb. 2016, doi: 10.1109/TPEL.2015.2420994.

[39] A. Kumar, M. Losito, M. Moradpour, and G. Gatto, “Current source gate driver for SiC MOSFETs in power electronics applications,” in *Proc. Int. Symp. Power Electron., Electr. Drives, Autom. Motion (SPEEDAM)*, Sorrento, Italy, Jun. 2022, pp. 523–527, doi: 10.1109/SPEEDAM53979.2022.9842111.

[40] M. Nauman and W. Shireen, “Efficient continuous control-set model-free predictive control of a grid-forming inverter with an LCL filter,” *IEEE Access*, vol. 13, pp. 157235–157248, 2025, doi: 10.1109/ACCESS.2025.3605731.

[41] A. Jain, A. K. Panigrahy, S. Saini, A. K. Bansal, and M. N. Bhukya, “Chef-based optimization algorithm (CBOA)-based global peak power tracking scheme for PV system,” *IEEE Access*, vol. 13, pp. 156246–156257, 2025, doi: 10.1109/ACCESS.2025.3606338.

[42] D. V. S. Reddy, M. Golla, and S. Thangavel, “A new soft-switching high gain DC–DC converter with reduced components realized by active clamp and coupled inductors,” *IEEE Trans. Consum. Electron.*, vol. 71, no. 2, pp. 2749–2761, May 2025, doi: 10.1109/TCE.2025.3576738.

[43] M. Dhananjaya, M. J. Sathik, S. Mekhilef, and M. L. Alghaythi, “New single-input dual-output converter for DC nanogrid application,” *IEEE Trans. Consum. Electron.*, vol. 71, no. 2, pp. 3294–3303, May 2025, doi: 10.1109/TCE.2025.3545578.

[44] S. Chaurasiya and B. Singh, “A dynamically adaptive rising-edge shifting frequency PWM implemented MPFT technique for portable EV charger development,” *IEEE Trans. Consum. Electron.*, vol. 70, no. 3, pp. 5363–5375, Aug. 2024, doi: 10.1109/TCE.2024.3438878.

[45] M. K. Senapati, C. Pradhan, S. R. Samantaray, and P. K. Nayak, “Improved power management control strategy for renewable energy-based DC micro-grid with energy storage integration,” *IET Gener., Transmiss. Distrib.*, vol. 12, no. 18, pp. 4159–4167, Sep. 2018, doi: 10.1049/iet-gtd.2018.5019.

Amit Kumar (Member, IEEE) received the B.Sc. and M.Sc. degrees in physics from the Sri Sathya Sai Institute of Higher Learning, India, in 2002 and 2004, respectively, and the Ph.D. degrees in physics and innovation sciences and technologies from the University of Cagliari, Italy, in 2010 and 2018, respectively. He held a visiting scientist position with the Center for Advanced Studies, Research, and Development in Sardinia (CRS4) from 2011 to 2014. He was a Visiting Researcher with the University of Lorraine, Nancy, France, in 2025, and Indian Institute of Technology Roorkee, Roorkee, India, in 2024. His career has included significant roles, such as participating in Erasmus+ Staff Mobility for teaching with the Center of Electronics, SDU, Denmark. He is currently an tenure-track Assistant Professor with the Department of Electrical and Electronic Engineering, University of Cagliari. He has made substantial contributions to several projects, including two funded by European Union, and has authored over 90 papers published in international peer-reviewed journals and conference proceedings. His main research interests include DC-DC converters, wide band gap devices, renewable energy systems, and electrical vehicle battery management systems. He is a dedicated member of the IEEE and the IES Technical Committee on Power Electronics, reflecting his engagement with key professional communities. He is listed among the World’s Top 2% Scientists by Stanford University, USA, in 2025.

Suganthi Ramasamy (Member, IEEE) received the B.E. degree in electrical and electronics engineering, the M.E. degree in power electronics and drives, and the Ph.D. degree in electrical engineering from Anna University, Chennai, India, in 2010, 2013, and 2023, respectively. She participated in Erasmus+ Staff Mobility for teaching with the Center of Electronics, SDU, Denmark. She is currently an Assistant Professor with the Department of Electrical and Electronic Engineering, University of Cagliari, Italy. Her research interests include power electronics, power converters, control algorithms, and the renewable energy sector. She is a member of the IEEE Society.

Sanjeevikumar Padmanaban (Senior Member, IEEE) received the Ph.D. degree in electrical engineering from the University of Bologna, Bologna, Italy, in 2012.

He is currently a Full Professor in electrical power engineering with the Department of Electrical Engineering, Information Technology, and Cybernetics, University of South-Eastern Norway, Norway. He has authored over 750 + scientific papers. He is a fellow of the Institution of Engineers, India, the Institution of Electronics and Telecommunication Engineers, India, and the Institution of Engineering and Technology, U.K., and a fellow of European Academy of Sciences, Belgium. He received the Best Paper cum Most Excellent Research Paper Award from IET-SEISCON’13, IET-CEAT’16, IEEE-EECSI’19, IEEE-CENCON’19, and five Best Paper Awards from ETAEERE’16 sponsored by Lecture Notes in electrical engineering, Springer book. He received the Lifetime Achievement Award from Marquis Who’s Who-USA 2017 for his contributions to power electronics and renewable energy research. He is listed among the World’s Top 2 Scientists by Stanford University, USA, in 2019. He received the IEEE Systems Council Outstanding Service Award 2025 for his contributions to visionary leadership and outstanding service to the IEEE Systems Council through transformative educational initiatives and global outreach. Also, he received the IEEE Bozenna Pasik-Duncan Humanitarian Mentorship Award 2025 for his mentorship that extends beyond professional excellence, making a human impact by spearheading inclusion, empathy, and opportunity across global technical communities. He is an Editor/Associate Editor/Editorial Board Member of refereed journals, in particular IEEE SYSTEMS JOURNAL, IEEE TRANSACTIONS ON INDUSTRY APPLICATIONS, IEEE ACCESS, *IET Power Electronics*, *IET Electronics Letters*, and *International Transactions on Electrical Energy Systems* (Wiley). He is the Subject Editorial Board Member of*Energy Sources*, *Energies* journal, MDPI, and the Subject Editor of *IET Renewable Power Generation*, *IET Generation, Transmission and Distribution*, and *FACETS* journal, Canada.

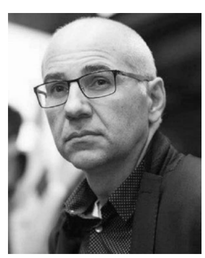

Gianluca Gatto (Senior Member, IEEE) received the degree in electrical engineering from the University of Cagliari, in November 1994. From October 1997, he was with the Department of Electrical and Electronic Engineering, University of Cagliari. Since 2019, he has been a Full Professor of converters, electrical machines, and drives. In 2003, he initiated a research activity with the Laboratory of Electromagnetic Compatibility (EMC), Department of Electrical and Electronic Engineering, University of Cagliari, and where he is currently the Scientific Director. The Laboratory offers EMC evaluation of electro-hydraulic actuators used in oil refineries, as well as assessment of the electromagnetic noise emission from power electronic converters employed in wind and solar power plants. He is also the Director of the POLILAB-interdepartmental laboratory, Faculty of Engineering. He is the author of more than 110 papers published in international peer-reviewed journals and conference proceedings. His research interests include power electronic converters, electrical machines, electromagnetic compatibility in industrial and hospital environments, management of cognitive buildings, innovative DC/DC converter topologies for electric vehicle battery management, and wide-bandgap technology. He is a Senior Member of the IEEE Society, with affiliations to the Industrial Electronics Society, the Electromagnetic Compatibility Society, and the Power Electronics Society.